Front. Earth Sci. 2022, 16(3): 757–773
https://doi.org/10.1007/s11707-021-0937-2

REVIEW ARTICLE

The influence of lunar surface position on irradiance of moon-based earth radiation observation

Yuan ZHANG, Shengshan BI (✉), Jiangtao WU

Key Laboratory of Thermo-Fluid Science and Engineering (Ministry of Education), School of Energy and Power Engineering, Xi'an Jiaotong University, Xi'an 710049, China

Abstract As a platform for longer-term continuous moon-based earth radiation observation (MERO) which includes reflected solar short-wave (SW) radiation and long-wave infrared (LW) radiation, the huge lunar surface space can provide multiple location choices. It is important to analyze the influence of lunar surface position on irradiance which is the aim of the present work based on a radiation heat transfer model. To compare the differences caused by positions, the site of 0°E 0°N was selected as the reference site and a good agreement of the calculation results was verified by the comparison with the NISTAR's actual detected data. By analyzing the spatial characteristics of the irradiance, the results showed that the irradiance on the lunar surface was of circular distribution and the instrument that was placed in the region of 65°W–65°E and 65°S–65°N could detect the irradiance most effectively. The relative deviation between the reference site and the marginal area (region of $>$ 65°S or 65°N or $>$ 65°W or 65°E) was less than 0.9 $mW \cdot m^{-2}$ and the small regional differences make a small-scale network conducive to radiometric calibration between instruments. To achieve accurate measurement of the irradiance, the sensitivity design goal of the MERO instrument should be better than 1 $mW \cdot m^{-2}$ in a future actual design. Because the lunar polar region is the priority region for future exploration, the irradiance at the poles has also been analyzed. The results show that the irradiance changes periodically and exhibits complementary characteristics of time. The variation range of irradiance for short-wave radiation is greater than long-wave radiation and the irradiance of SW reaches the maximum at different times. The MERO at the polar region will provide valuable practical experiment for the follow-up study of the moon-based earth observation in low latitudes.

Received May 27, 2020; accepted July 8, 2021

E-mail: bss@mail.xjtu.edu.cn

Keywords irradiance, earth observation, moon-based, lunar surface position, NISTAR

1 Introduction

Understanding the balance between incoming solar radiation and outgoing radiation is essential to our ability to predict global climate change. The incoming radiation mainly comes from solar radiation and the outgoing radiation is reflected solar shortwave (SW: 0.2–5 μm) radiation and longwave infrared (LW: 5–200 μm) radiation, respectively. At present, the incoming and outgoing radiation observation for Earth's radiation budget (ERB) is mainly based on satellite-based platforms with dedicated instruments, such as Clouds and the Earth's Radiant Energy System (CERES) onboard the Terra and Aqua satellites (Wielicki et al., 1996). The earth radiation budget (ERB) at the top of earth's atmosphere is a balance of the energy earth gains from the sun (F_0) against energy lost to space through the reflection of short-wave solar radiation (F_S) and the emission of longwave thermal radiation (F_L). So, the ERB can be discussed by monitoring the F_0, F_L, F_S (Liang, 2018) and, here, we focus on F_L and F_S. Compared to artificial satellites, the moon has many features to recommend it as a suitable platform for realizing the goal of earth outgoing radiation observation, and the difference in orbital height for a satellite-based platform and a Moon-based platform makes them have complementary characteristics in observation. For the polar-orbiting-satellite, the limited temporal sampling may neglect some variations of small time-scales, which could be important for studying the earth radiation budget. However, the moon-based platform can provide continuous observations of the majority of observed points with continuously changing angles, which enable the recording of long-term time-series data covering all local times and all seasons in a year (Pallé and Goode, 2009; Karalidi et al., 2012). The generated data

from a geostationary orbit satellite could help to make up for the lack of temporal samples of the 60°S–60°N region on earth, but it is restricted by limited longevity and observable area. Due to the limit of synchronous rotation, the moon always faces earth with its nearside. So the moon is a unique platform for the study of the disk-wide radiation balance budget of earth. Besides, the long life-cycle and stable orbit of the moon will allow for a substantially longer longevity for a moon-based observation instrument. The Deep Space Climate Observatory (DSCOVR) situated at the Earth-Sun Lagrange Point (L1) can observe the long-wave (LW) and short-wave (SW) irradiance from the illuminated side of the Earth with high accuracy and sampling frequency, but due to limitation of the orbit, only about 92%–97% of the sunlit Earth is visible to NISTAR (Su et al., 2020). The lunar platform can provide images of the earth at a hemispherical scale and high temporal sampling observation for the earth, which will be a powerful supplement to calibrate the data of satellites. Moreover, because the lunar surface has a large load capacity, various types of equipment can be placed to collect various types of data. In addition, compared to the current satellite-based platforms, the advantages of moon-based platform also have been summarized and clarified in existing literature (Huang, 2008; Guo et al., 2018, 2020; Ye et al., 2018a, 2018b, 2019).

A more accurate radiometric calibration can also be achieved on the lunar surface due to the stable selenographic radiation environment. Of course, the lunar surface will also face many challenges, such as huge temperature differences, highly vacuum space environments and energy. Besides, the long-term work of the current lunar instrument shows that the impact of moon dust is within the expected range (Durante and Cucinotta, 2011; Lohmeyer and Cahoy, 2013).

Since the utilization of moon-based platforms to observe the earth's outgoing radiation is a relatively new research region, the previous work mainly focuses on the feasibility and effectiveness of moon-based earth observation (Johnson et al., 2007; Pallé and Goode, 2009), the viewable range and its changes (Ye et al., 2018a, 2018b), observation geometric conditions (Wang et al., 2019), observation methods and error analysis (Guo et al., 2018), and the simulation of the land surface parameters (Yuan and Liao, 2019, 2020). The purpose of this work is to analyze the position difference of irradiance, so as to provide a reference for the parameter design and position selection of the detector. Huang (2008) pointed out that the changes in the lunar surface temperature are mainly controlled by terrestrial radiation during the lunar nighttime by analyzing the Apollo 15 heat flow experiment data, which provides a good support for the use of moon-based platform to study earth radiation. Ye et al. (2018a, 2018b) pointed out that the maximum nadir point's latitudinal and longitudinal difference on the moon surface is about 0.3°, the maximum viewing angle difference of the earth is about 0.24° compared with the selenocentric case. In addition, the maximum observation elevation angle difference is about 0.27° caused by different lunar positions and different lunar surface positions also cause changes in the observation duration, energy requirements, and lunar environment of a lunar-based platform. Duan et al. (2019) build an irradiance estimating model for terrestrial radiation at the entrance pupil of a simplified single-pixel moon-based earth radiation observatory instrument by taking the CERES data products and angular distribution models into account. Moreover, the effect of variation in orbit on irradiance was analyzed and 4 sites (80°E, 0°N; 80°W, 0°N; 0°E, 81°N; 0°E, 81°S) are considered for the impact of location. The average radius of the moon is 1738 km, about 1/4 of the earth's radius, and the surface area is about 37.9×10^6 km^2. The surface of the moon can be divided into two major terrains: mare and highland. The mare is a wide plain, accounting for about 17% of the lunar surface area. The majority of the mare is distributed on the nearside of the moon, accounting for about half of the entire nearside hemisphere. Highlands refer to the areas where the lunar surface is higher than the Mare, generally about 2–3 km higher than the lunar level, and the area accounts for about 83% of the moon's surface area. Different topographic features and the huge surface space of the moon provide a large number of options for the position of MERO instruments. The irradiance is the radiation which will finally arrive at the detection element of the instrument (Luther et al., 1986), so the entrance pupil irradiance of the instrument will vary with the placement position, but few studies involve the quantitative analysis of the influence of lunar surface position on irradiance. Therefore, it is necessary to analyze the influence of lunar surface position on irradiance of moon-based earth radiation observation.

In this work, a radiation heat transfer model directly based on the law of energy conservation and thermal radiation was used to calculate and analyze the spatial characteristics of the irradiance. Taking the lunar surface site 0°E 0°N as the reference, we analyzed the magnitude, period, and range of the irradiance and the influence of lunar surface position on irradiance. The lunar polar region was selected as an application of this model and the irradiance were further analyzed. The MERO at the polar region will provide valuable practical experience for follow-up study of moon-based earth observation in low latitudes.

2 Model

2.1 Geometric model

To determine the observable region to the earth's top of atmosphere (TOA) from the lunar surface and the energy contribution of different regions to the lunar irradiance, it is necessary to discretize the surface of the earth's TOA.

Since the integral method is used in this work, the method of grid discretization does affect the simulation result and we also discussed the relationship between grid size and simulation accuracy in Section 3.1. The resolution of satellite-based data products currently used to study the Earth's energy balance is usually a grid of 1° latitude×1° longitude. Therefore, for the unity of the data, we also use a grid of 1° latitude × 1° longitude to simulate. So, a discretization method paralleling earth's longitude and latitude line was adopted in this work. Figure 1 shows the observation geometry model for the MERO

In the Fig. 1, O_m and O_E are the center of the earth and the moon, respectively. F and G are the nadir of the earth on the lunar surface and the moon on the earth's TOA, respectively. Lines ED and HC are the inner common tangent of the earth's TOA and the moon, the angle γ is half of the angle $\angle CO_ED$. A_i is the arbitrary point on the lunar surface and the angle σ is the angle between the line O_mA_i and O_mO_E. B_i is the arbitrary mesh node on the earth's TOA, $\vec{n_l}$ is the normal line of the region at the mesh node B_i, ϕ_i is the angle between the vectors $\overrightarrow{B_lA_l}$ and $\vec{n_l}$, and $\overrightarrow{O_EA_l}$ is the vector of the arbitrary point A_i in the earth-centered earth-fixed coordinate system (Lieske, 1979; Petit and Luzum, 2016), $\overrightarrow{O_EB_l}$ is the vector of the arbitrary mesh node B_i in the earth-centered earth-fixed coordinate system. The position data are derived from the ephemeris DE430 provided by Jet Propulsion Laboratory (JPL) and the definition of coordinate system and mutual conversion relationship can refer to references (GSFC, 2008; Folkner et al., 2008; Ye et al., 2018a, 2018b). To have a hemispherical view of the earth, the position for MERO on the lunar surface should be set on the spherical crown corresponding to the angle $\angle EO_mH$, that is, the following relationship must be satisfied:

$$\sigma < \gamma, \tag{1}$$

$$\cos\sigma = \cos\theta\cos\theta_F\cos(\phi-\phi_F) + \sin\theta\sin\theta_F, \tag{2}$$

$$\cos\gamma = \frac{R_e + R_m + h}{D_{me}}, \tag{3}$$

where θ and ϕ are the latitude and longitude of A_i, θ_F, and ϕ_F are the latitude and longitude of point F. R_e and R_m are the radius of the earth and the radius of the moon, respectively (where the radius of the earth is the radius at the earth's equator), h is the thickness of the atmosphere, D_{me} is the distance between the center of earth and the center of moon.

At the same time, if the mesh node B_i can be observed at point A_i, the following relationship must be satisfied:

$$\angle\phi_i \leqslant \frac{\pi}{2}. \tag{4}$$

2.2 Radiation heat transfer model

Usually, the instantaneous field of MERO-viewed of the earth's TOA consists of part bright surface and part dark surface. The bright surface is the area illuminated by the sun, so it not only emits outgoing long-wave radiation (5–200 μm) (OLR), but also includes the outgoing short-wave (0.2–5 μm) radiation reflected by the earth's TOA (OSR). The dark surface only has the OLR. Limited in its own synchronous rotation, the nearside of the moon always faces earth. Since the rotation cycle of the earth is 24 h, the nearside of the moon can sample the whole earth in one day (Guo et al., 2018; Li, Guo et al., 2019; Huang et al., 2020). Figure 2 is the model for calculating the irradiance arrived at the lunar surface from the earth's TOA. Point A is the arbitrary position where the whole earth can be seen on the lunar surface. dW and dZ represent the unit area of the earth's TOA and the lunar surface, respectively, $\vec{n_1}$, $\vec{n_2}$ are the normal vectors of dW and dZ, respectively. L1 is the distance of the center H of dW and the center A of dZ. α_1,α_2 are the angles between $\vec{n_1}$, $\vec{n_2}$ and AH, respectively. Angle β is the angle between the sunlight vector $\vec{sun}$ and the $\vec{n_1}$, h is the thickness of the atmosphere.

The Earth Radiation Budget (ERB) is among the most fundamental climate change parameters to be monitored. The Earth Energy Imbalance is a relatively small value but it is the direct driver of climate change on earth. According to the conservation of energy, we can get Eq. (5) (Stephens et al., 2015; Peyrou-Lauga, 2017; Liang, 2018) and this

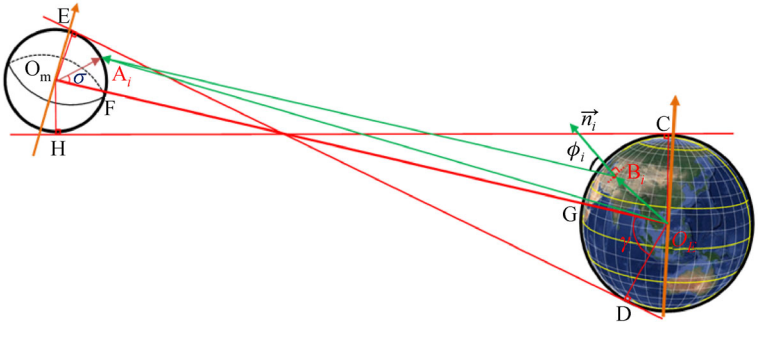

Fig. 1 The observation geometry model for the MERO.

method is often used to calculate and analyze the influence of external heat fluxes on spacecraft (Clark and Anderson, 1965; Mudawar, 2001; Gilmore, 2002; Tsai, 2004):

$$F_{\text{net}} = F_0 - F_S - F_L = F_0(1-\alpha_{\text{TOA}}) - F_L, \tag{5}$$

where α_{TOA} is the planetary albedo, defining the fraction of the incoming solar energy reflected by earth back into space (Liang, 2018). F_{net} is the net radiation on the earth's TOA between incoming and outgoing radiative fluxes.

For the irradiance of OLR and OSR received by per unit area on lunar surface, it can be calculated by

$$\text{OLR}: Q_{\text{OLR}} = \int_A \int_\Omega F_L \ \mathrm{d}A\mathrm{d}\Omega, \tag{6}$$

$$\text{OSR}: Q_{\text{OSR}} = \int_A \int_\Omega F_0 \cdot \alpha_{\text{TOA}} \ \mathrm{d}A\mathrm{d}\Omega. \tag{7}$$

Since the earth is not a black body, the reflected radiation by the earth's TOA not only depends on the incident spectrum and the incident direction, but is also related to the various characteristics of the reflective surface and the direction of observation. To simplify the model, we assume that the reflection of sunlight from the earth's TOA is diffuse, regardless of the characteristics of bidirectional reflectance, and the reflection obeys the law of cosines. The irradiance of OLR and OSR can be derived by the following discrete summation equations (Holman, 2002; Yang and Tao, 2006):

$$Q_{\text{OLR}} = \sum_N F_{L,i} \int_{W_{\text{OLR}}} \frac{\cos\alpha_1 \cos\alpha_2}{\pi L_i^{\ 2}} \sqrt{a^2\cos\theta^2 + b^2\sin\theta^2} \cdot \cos\theta \mathrm{d}\varphi \sqrt{a^2\sin\theta^2 + b^2\cos\theta^2}\mathrm{d}\theta, \tag{8}$$

$$Q_{\text{OSR}} = \sum_M F_{0,i} \cdot \alpha_{\text{TOA},i} \int_{W_{\text{OSR}}} \frac{\cos\beta\cos\alpha_1\cos\alpha_2}{\pi L_i^{\ 2}} \cdot \sqrt{a^2\cos\theta^2 + b^2\sin\theta^2}\cos\theta\mathrm{d}\varphi \cdot \sqrt{a^2\sin\theta^2 + b^2\cos\theta^2}\mathrm{d}\theta, \tag{9}$$

where a and b are the equatorial radius and polar radius of the earth's TOA. θ is the latitude of the center of the node area of the earth's TOA. ds is the arc length, dθ is the latitude unit increment, dφ is the longitude unit increment, and L is the distance from the mesh node B_i to the center of the earth (detailed description see Section 2.1) (Holman, 2002; Yang and Tao, 2006).

In Eqs. (8) and (9), $F_{\text{L},i}$, $F_{0,i}$, and $\alpha_{\text{TOA},i}$ represent the emitted longwave radiative fluxes, solar constant and planetary albedo on the earth's TOA, respectively. Figure 3(a) shows the global monthly average OLR time series values of several satellite-based data products from September 2002 to January 2018 (Fig. 3(a)), and Fig. 3(b) shows the average outgoing long-wave radiation at TOA in $\text{W}\cdot\text{m}^{-2}$ from CERES for February 15, 2017. it can be seen from the Fig. 3 that the global monthly average OLR shows periodic changes and the range of change for OLR is about 235–245 $\text{W}\cdot\text{m}^{-2}$. Figure 3(b) shows that the OLR is the largest at the equator and smallest in the polar regions. The solar constant, total solar irradiance integrated over all wavelengths at the mean earth–sun distance, and it is generally considered to be between 1361 and 1364 $\text{W}\cdot\text{m}^{-2}$ (Kopp, 2016). The planetary albedo $\alpha_{\text{TOA},i}$ is the fraction of incident global mean solar flux reflected to space and two approaches were used for estimating planetary albedo: 1) satellite remote sensing; 2) ground measurement of earthshine by observing the moon. With the development of algorithms and instruments, the accuracy of planetary albedo is constantly improving and its value currently varies between 0.29 and 0.3 (Liang, 2018).

2.3 Calculation process and simplification

Figure 4 shows a flowchart for calculation of radiation heat transfer between the earth's TOA and the moon. The first step is to set the time range, time step, and lunar surface resolution. The second step is to discretize the earth's TOA at a resolution of 1°×1° and generate the coordinate vector in the same coordinate and time system by using the JPL Ephemeris and the earth orientation parameter (EOP)

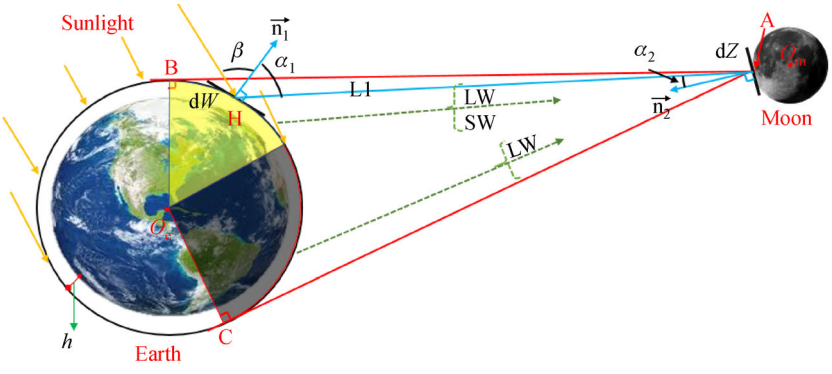

Fig. 2 Irradiance calculation model between the earth's TOA and the moon.

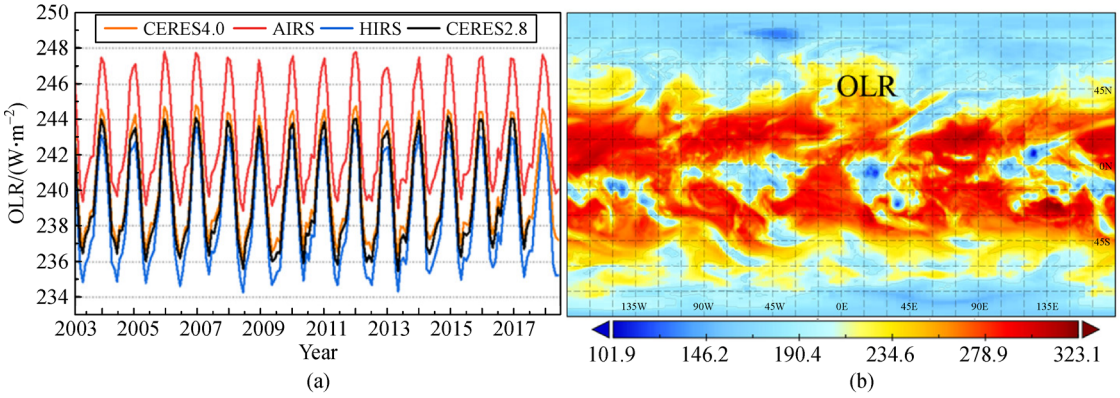

Fig. 3 (a) The global monthly average OLR time series values from September 2002 to January 2018; (b) The average outgoing long-wave radiation at TOA in W·m^{-2} from CERES for February 15, 2017.

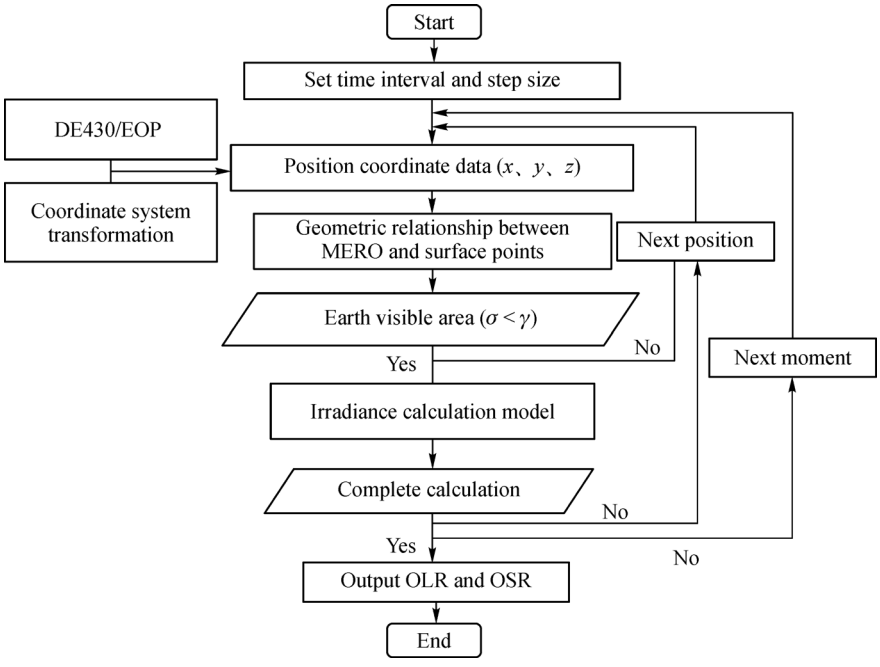

Fig. 4 Flowchart for calculation of irradiance.

provided by International Earth Rotation and Reference System Service (IERS). The third step determines the long-wave (LW) and short-wave (SW) visible node area according to the geometric relationship. The fourth step calculates the irradiance of OLR and OSR received on the lunar surface. Since point F (Fig. 1) changes in the area of 8°W–8°E and 7°S–7°N, the lunar surface site (0°E, 0°N) is selected as the reference point to analyze the influence of lunar surface position on irradiance of moon-based earth radiation observation.

To simplify the analytical calculation process, in this work, the model is simplified as follows.

1) The moon is assumed to be a sphere with a radius of 1738 km, ignoring the influence of the lunar terrain and regardless of the influence of the space background radiation.

2) The earth is assumed to be a spheroid with the equatorial radius as the long axis and the polar radius as the short axis.

3) The earth's TOA is a diffuse surface, and the radiation outgoing at different locations is uniform.

3 Results and discussion

3.1 Magnitude, sensitivity and model validation

The resolution of earth's TOA directly affects the range of

the visible area from the lunar surface point, and then affects the magnitude of the irradiance. So, it is necessary to discuss the relationship between the grid size on the earth's TOA and the simulation accuracy. Figure 5 shows that the relationship between absolute deviation of irradiance (LW) with the resolution earth's TOA (the moon surface position is 0°N, 0°E and the distance is the average distance between the earth and the moon). It can be seen from Fig. 5 that when the resolution changes from 0.5°×0.5° to 1.0°×1.0°, the change in irradiance is 0.098 $mW \cdot m^{-2}$ and this value is about 0.15% of the irradiance (LW = SW = 0.07 $W \cdot m^{-2}$). As the resolution of the grid increases to 2.0°×2.0°, the change of irradiance is 0.45 $mW \cdot m^{-2}$ and this value is 4.6 times of that at the resolution of 1.0°×1.0°. Considering the influence of the distance between the earth and the moon, regional characteristics of the earth's outgoing radiation, the calculation time cost, the resolution of the satellite-based detection data, the following analysis results, and the main purpose of this work, the earth's TOA was discrete as a node of 1° latitude×1° longitude in the calculation of Eqs. (8)–(9).

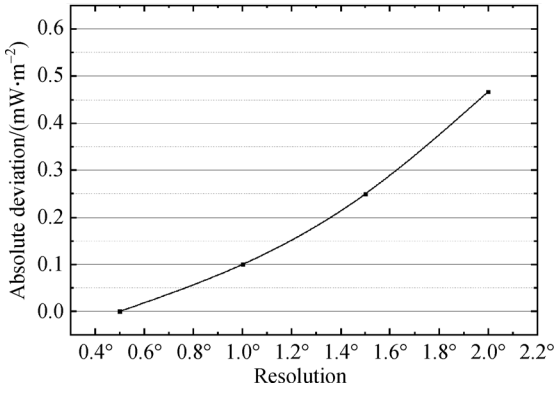

Fig. 5 The relationship between absolute deviation of irradiance with the resolution of earth's TOA.

The magnitude and the range of variation of the irradiance is an essential factor for the design of the MERO instrument. Figure 6 shows the envelope diagram of the irradiance at the reference point from 1998 to 2017 and the max and min in Fig. 6 represent the diurnal variation irradiance extremes of the OSR and OLR, respectively. From the Fig. 6(a), we can see that the OLR and OSR exhibit periodic changes mainly caused by the special operation law among the sun, the moon, and the earth. The peak energy of the OSR is about 0.01 $W \cdot m^{-2}$ higher than the OLR, which is caused by strong direct sunlight. For OLR, the average value is 0.067 $W \cdot m^{-2}$ and the range of variation is 0.059–0.077 $W \cdot m^{-2}$, and for OSR, the average value and the range of variation are 0.030 $W \cdot m^{-2}$ and 0–0.088 $W \cdot m^{-2}$, respectively.

The envelope diagram of the sum of OLR and OSR is shown in Fig. 6(b). The period of the total amount of

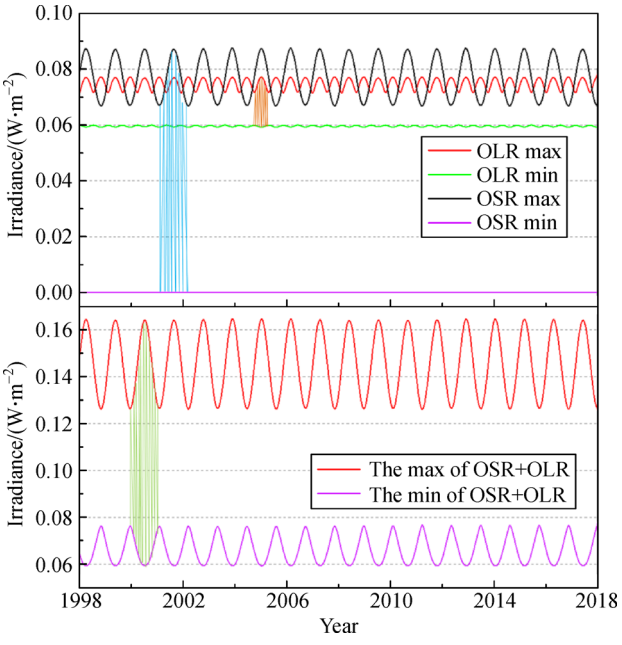

Fig. 6 The envelope diagram of the irradiance received at the reference point from 1998 to 2017. This max and min represent the diurnal variation irradiance extremes of the OSR and OLR, respectively.

irradiance extremes is about 1 year, and the maximum, minimum, and average value are 0.164, 0.059, and 0.097 $W \cdot m^{-2}$, respectively. The received irradiance on the lunar surface depends on the angle factor and surface radiant characteristics at any given time. To determine the sensitivity of the irradiance, the increase of the irradiance corresponding to the change in the unit of emitted radiative fluxes is defined as MERO sensitivity (MEROS). Figure 7(a) shows the MEROS at the reference point in October 2017. When the change of the emitted radiative fluxes on the earth's TOA is 5.00 $W \cdot m^{-2}$, OLR and OSR increase by an average of 2.10% and 1.22%, respectively; for long periods of 18.6 years or longer, the irradiance of OLR and OSR increased by an average of 2.11% and 1.24%, respectively.

The DSCOVR, launched on February 11, 2015, is a space weather and science spacecraft situated at the Earth-Sun Lagrange Point (L1), and the spacecraft is managed by National Oceanic and Atmospheric Administration. DSCOVR is designed to continuously monitor the sunlit side of the earth, being the first earth observing satellite at the Lagrange-1 (L1) point, ~1.5×10^6 km from earth. The National Institute of Standards and Technology Advanced Radiometer (NISTAR) onboard the DSCOVR provides continuous full-disk global broadband irradiance measurements over most of the sunlit side of the earth (Su et al., 2020). Therefore, the NISTAR can provides a meaningful reference and verification for the realization of MERO. In addition, it is worth noting that the magnitude of irradiance measured by the NISTAR instrument on DSCOVR is also

on the order of 10^{-3} W·m^{-2} and the accuracy of the detector is 1.5% or better. It shows that the current detection technology can realize the detection of the irradiance on the lunar surface. Figure 7(b) shows the irradiance from the earth's TOA at different heights, that is, instrument's entrance pupil irradiance when the entire earth's TOA is within the field of view of the instrument. It can be seen from Fig. 7(b) that from the low orbit (600 km) to the point L1 (1.5×10^6 km), the change of the irradiance for the LW and SW are from 287.21 W·m^{-2} to 4.3 mW·m^{-2} and from 451.53 W·m^{-2} to 4.6 mW·m^{-2}, respectively, and the sum of LW and SW is from 738.74 to 8.9 mW·m^{-2}.

The calculation method used in Fig. 7(b) is consistent with the model in this work and the main difference is the variation of the height of the orbits. Since the NISTAR at point L1 is always facing the Earth illuminated by the sun, the measured LW and SW radiation comes from the illuminated side of the earth. The NISTAR on the DSCOVR views the Earth as one pixel in three bands (A: 0.2–100 μm, B: 0.2–4 μm, C: 0.7–4 μm) plus a reference (D: 0.3–1 μm). NISTAR's science goal is to provide measurements of the total outgoing radiation from the earth in the wavelength range of 0.2 μm to 100 μm with an accuracy of 1.5% or better. To verify the correctness and usability of the calculation model in this work, it is assumed that the instrument is also located at a large circle which the center is the earth, and the radius is the distance of the L1 point from the earth (1.5×10^6 km), and the surface is also illuminated by sunlight. Figure 8 shows that the SW and total earth irradiance at L1 height calculated by the model in this work in 2017, and SW and total earth irradiance received by NISTAR from April to December 2017. It can be seen from Fig. 8 that the calculation results of this model from April to December in 2017 are in good agreement with the actual detection results of NISTAR, and the detection result of NISTAR indicates the total earth irradiance and SW earth irradiance vary from 9 to 10.5 mW·m^{-2} and from 4 to 6 mW·m^{-2} in 2017. The consistency of SW is slightly better than that of LW. The simulation value of the irradiance is smaller than the actual detection value of NISTAR by no more than 0.5 mW·m^{-2}, and the existence of this difference is mainly due to the change of scene of the earth's TOA.

3.2 Spatial characteristics of the irradiance

3.2.1 Different location at the same time

The huge surface space of the moon provides multiple choices for the location of MERO and the irradiance varies with the lunar position, so it is necessary to study the spatial characteristics of irradiance on the lunar surface. In this work, the contour distribution of OLR and OSR at the moments A (October 8, 2017, 7 am — time of maximum earth-moon distance) and B (October 23, 2017, 6 pm — time of maximum SW irradiance) in October 2017 were calculated at different positions on the lunar surface and the results are shown in Fig. 9. According to the calculation model in Section 2 and the definition of irradiance, the irradiance at different lunar positions depends on the geometric relationship between that lunar position and the earth's TOA. The changes in the resolution of the lunar surface and the earth's TOA have different effects on irradiance. The change of earth's TOA resolution will directly affect the visible range of the lunar site, which in turn affects the angle factor in Eqs. (8)–(9) and the irradiance. However, the different lunar positions will only change the geometric relationship and do not have an essential impact on irradiance. The purpose of the analysis in this section is to obtain the overall distribution characteristics of irradiance on the near-side of the moon and the change in resolution does not change the overall distribution of irradiance. In addition, after obtaining the overall irradiance distribution, we will use a 1° resolution grid for further analysis. It can be seen from Fig. 9 that the irradiance received on the lunar surface presents a circular distribution which decreases from the maximum at the center site (0°E, 0°N) to the surrounding direction. In

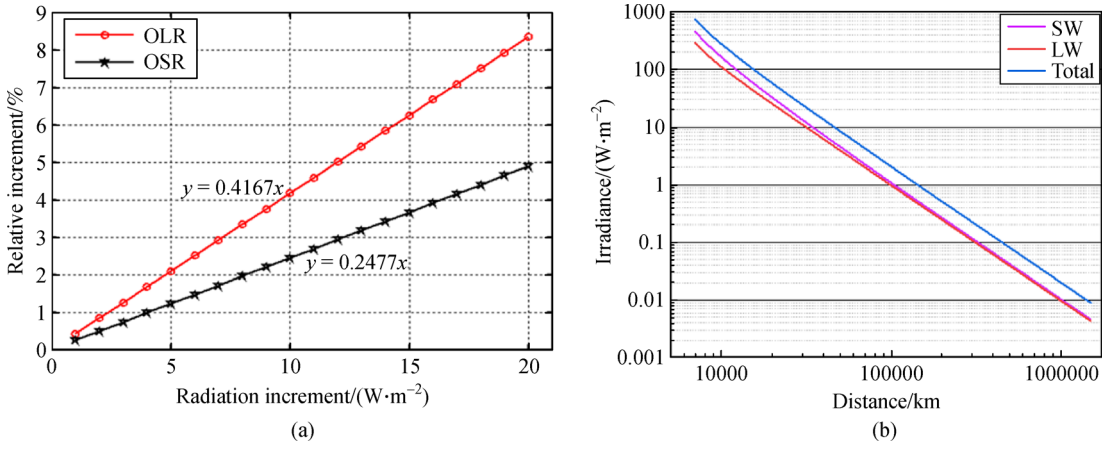

Fig. 7 (a) MEROS at the reference point in October 2017 and (b) the irradiance at the different positions from the low orbit (600 km) to the point L1 (1.5×10^6 km).

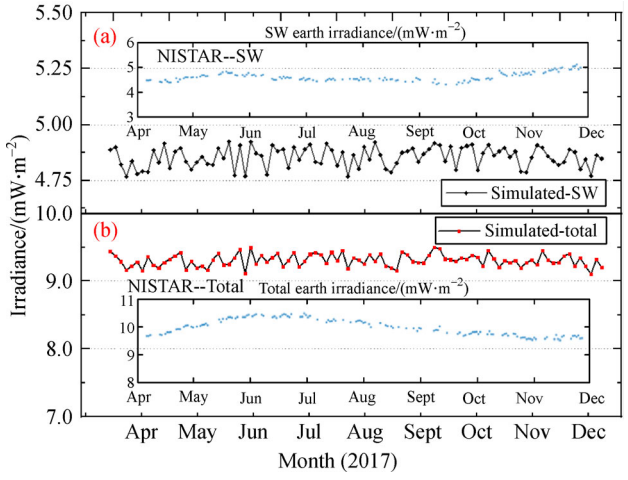

Fig. 8 NISTAR yearly variation (Image Source: NASA website), and the SW and total earth irradiance calculated by the model in this paper.

Fig. 9(a) the central maximum value region is mainly the nadir point region of the earth, and the maximum value region is mainly located in 10°W–10°E and 10°S–10°N in the 18.6-year period. If the moon-based earth radiation observation instrument was placed in the region of 65°W–65°E and 65°S–65°N, the instrument will receive OLR more efficiently. Figure 9(b) shows a similar result for the distribution of the OSR, but the central area will change slightly along the longitude. The distribution characteristics of OLR and OSR are consistent with that of Fig. 9 and the difference is only the change of the center position and the energy value. Therefore, we selected points on 0°N latitude and 0°E longitude for further analysis. The permanent visible area of the moon to the earth's TOA is in the region of 80.5°W–80.5°E and 81.5°S–81.5°N on the nearside of the moon, when the moon-based earth radiation observation instrument is placed in the region 65°W–65°E and 65°S–65°N, it can guarantee the permanent detectability of the Earth and ensure that the MERO instrument can detect the earth's outgoing radiation more effectively.

To analyze the difference of the irradiance received on different lunar positions, the moment B in Fig. 9 is selected for the OSR and 1° resolutions is used along the 0°E longitude from north to south and along the 0°N latitude from west to east. Figures 10(a) and 10(b) show the irradiance of the OSR at different positions and the relative deviation from the reference point. It can be seen from Fig. 10 that the maximum value of OSR is 0.07288 W·m^{-2}, and the minimum value is 0.07224 W·m^{-2} obtained in the edge region, and the variation range is about 0.88%. The closer to the edge area, the greater the deviation and the relative deviation of the OSR between the reference point and the edge region are 0.9%, 0.76%, 0.84%, and 0.84% in positions Nb, Sb, Wb, and Eb (N, S, W, and E represent North, South, West, and East, b is the boundary), respectively (Figs. 10(a) and 10(b)).

Similarly, the moment A in Fig. 9 is selected for the comparison for the OLR. Figures 11(c) and 11(d) show the irradiance of the OLR at different positions and the relative deviation from the reference point. It can be seen from Fig. 11 that the variation range of OLR is 0.07223–0.07285 W·m^{-2}, and range of change is about 0.85%. The relative deviation of the OLR between the reference point and the edge region are 0.83%, 0.918%, 0.913%, and 0.9% in positions Nb, Sb, Wb, and Eb, respectively (Figs. 11(a) and 11(b)). In summary, the influence of the curvature of

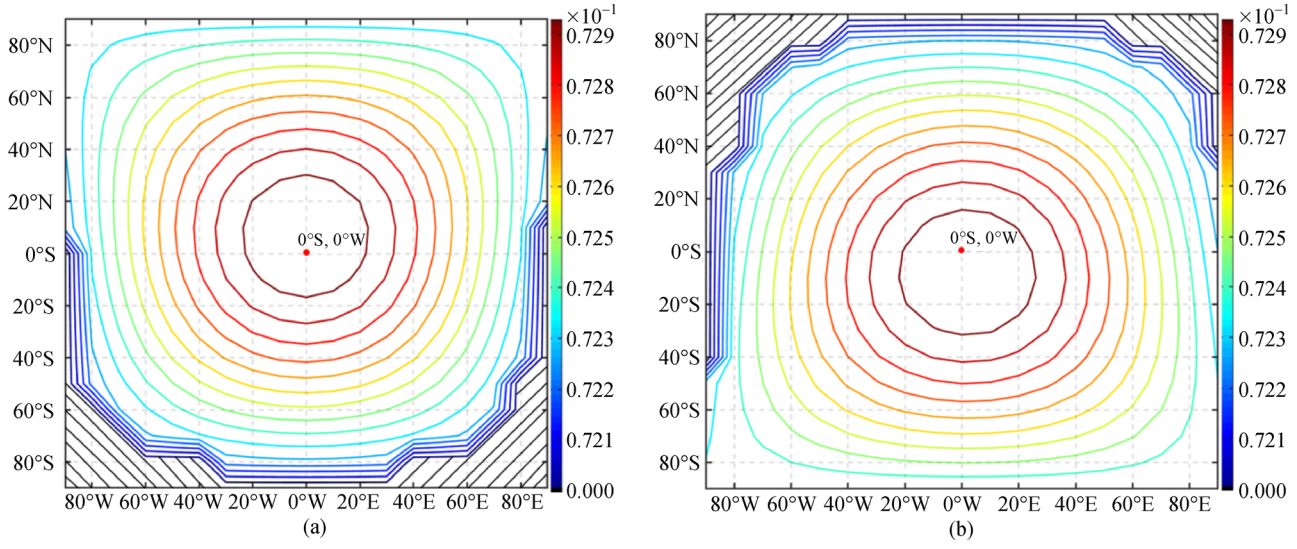

Fig. 9 The contour distribution of OLR and OSR at A and B moments in October 2017 on the lunar surface (the slashed black area indicates the invisible regions to the earth's TOA).

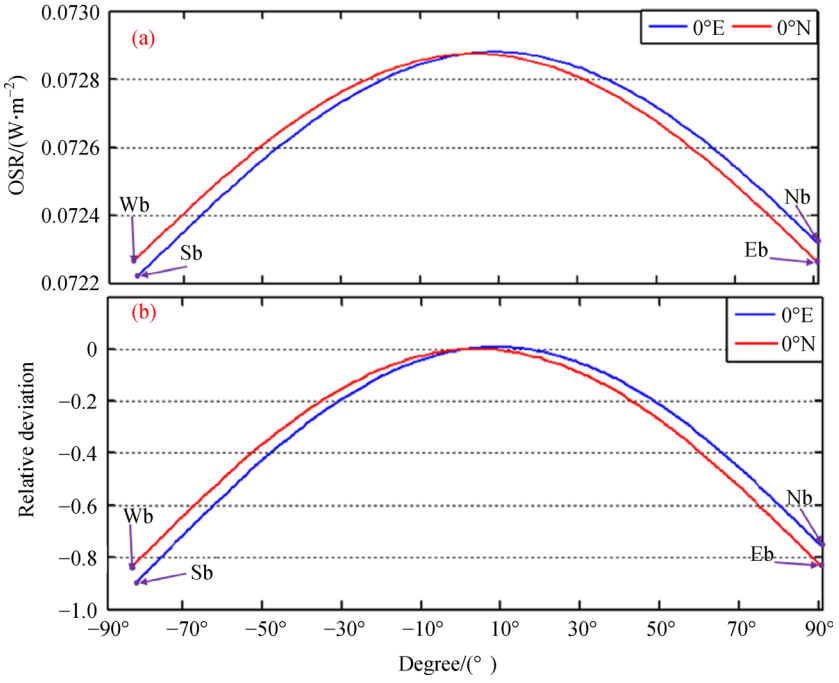

Fig. 10 (a) The irradiance of the OSR at lunar different positions and (b) the relative deviation from the reference point in the moment D in October 2017.

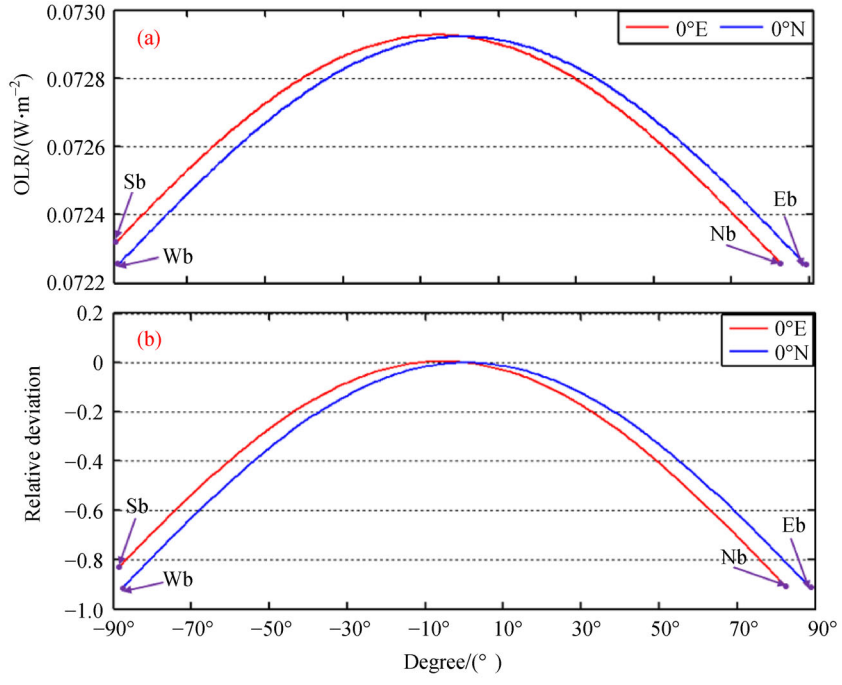

Fig. 11 (a) The irradiance of the OLR at lunar different positions and (b) the relative deviation from the reference point in the moment A in October 2017.

the lunar surface cause the change of the irradiance of OSR and OLR at lunar different positions are relatively small, and the relative deviations from the reference point are below 0.9% and 0.92%, respectively.

3.2.2 Different locations at the different time

Due to the special laws of motion between the sun, the earth and the moon, different lunar places see different

positions of the earth at different times, so the irradiance received on the lunar surface not only vary with location but also with time. Figure 12 shows the change of the irradiance of OSR along the 0°E longitude from north to south and along the 0°N latitude from west to east with the 1° resolution. It can be seen from Fig. 12 that the trends of the overall OSR in one orbital period are similar, and there are a maximum value and a minimum value reached at the same time, which is caused by the difference of positions. At the extreme value time, the variation range of OSR is 0.0723–0.0729 $W \cdot m^{-2}$ and the range of change is about 0.83%. The deviation of the OSR at different positions from the reference point is different. The deviation variation ranges on 0°E and 0°N are -6×10^{-4}–0.8×10^{-4} and -6.5×10^{-4}–0.3×10^{-4} $W \cdot m^{-2}$, respectively, and the ranges are approximately 0.933% and 0.892% of the results of the OSR at reference point.

Similarly, Fig. 13 shows the change of the irradiance of OLR along 0°E longitude and 0°N latitude in October 2017. First, it can be seen from Fig. 13 that the OLR exhibits an approximate sinusoidal law change, and the variation at different positions have a good consistency. Second, the variation ranges of OLR along 0°E longitude and 0°N latitude at the maximum value moment are 0.07225–0.07293 and 0.07234–0.07292 $W \cdot m^{-2}$, respectively, and the ranges of change are 0.941% and 0.802%, respectively. The variation ranges at the minimum value moment are 0.05925–0.05974 and 0.05929–0.05974 $W \cdot m^{-2}$, respectively, and the ranges of change are 0.827% and 0.759%, respectively. The deviation variation range are -6.3×10^{-4}–0.3×10^{-4} and -6.8×10^{-4}–0.3×10^{-4} $W \cdot m^{-2}$, respectively, and the variation range accounts for 0.8% and 0.85% of the OLR at reference point, respectively.

Since the angle between the earth's equator and the lunar orbital plane exits an 18.6 year cycle, it is necessary to analyze the variation characteristics of OLR and OSR on the time scale of an 18.6 year cycle. Figure 14 (the drawing method is the same as that of Fig. 6) shows the envelope diagram of the change of the irradiance of OLR and OSR at 0°N0°E and 70°N0°E. First, the change period of OLR and OSR itself are approximately one month and there is a small deviation between different locations. The extreme value of OLR and OSR in every month also shows obvious periodicity: the former is half a year and the latter is one year, which is consistent with Fig. 6. Secondly, the variation ranges of OLR and OSR at different positions are 0.05885–0.07724 and 0–0.0876 $W \cdot m^{-2}$, respectively. The relative deviation of OLR and OSR at two different zones of the lunar surface along the 0°E longitude relative to the reference point and the average of the different positions is shown in Table 1. The relative deviation from the reference point and the average are less than 0.9% and 0.8%, respectively, so the difference in position has a consistent effect on the irradiance of OLR and OSR. The change in relative deviation caused by different positions is relatively stable in the long period, which is advantageous for stable and accurate detection of earth radiation. On 0°N latitude, the variation of the OLR and OSR is like that on the 0°E longitude, and the relative deviations of OLR and OSR are also less than 0.9%.

From the previous analysis, it can be seen that the irradiance is distributed in a ring shape with the reference point (0°E, 0°N) as the center, and the relative deviation

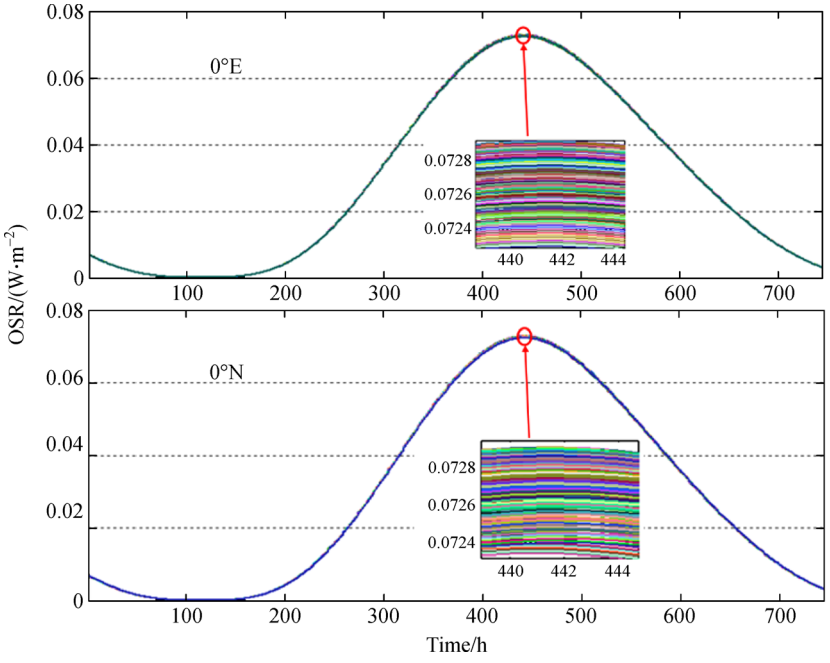

Fig. 12 The variation of the irradiance of the OSR at different positions along 0°E and 0°N in October 2017 at a resolution of 1°.

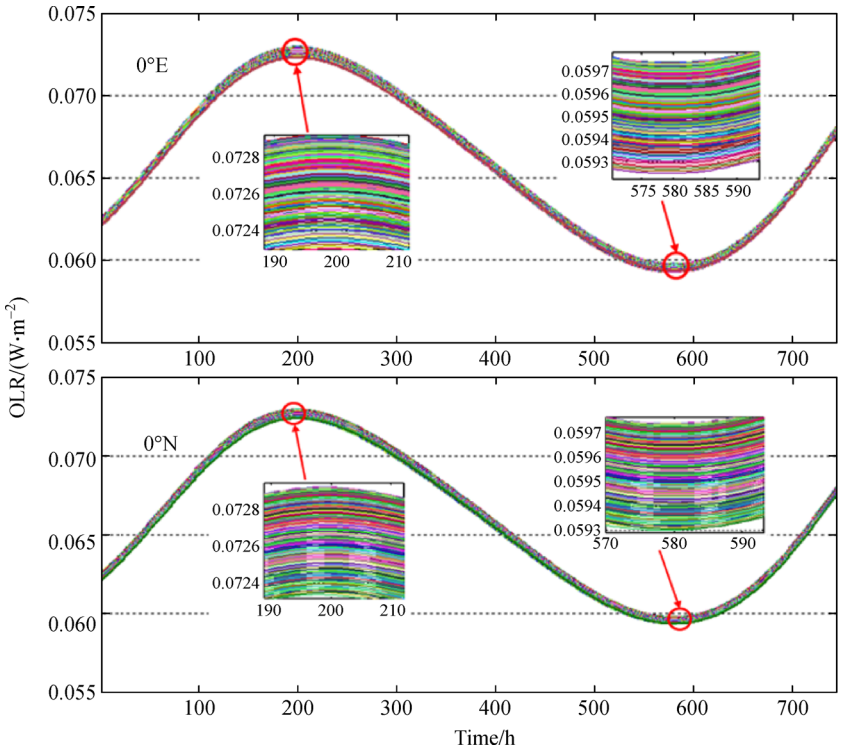

Fig. 13 The variation of the irradiance of the OLR at different positions along 0°E and 0°N in October 2017 at a resolution of 1°.

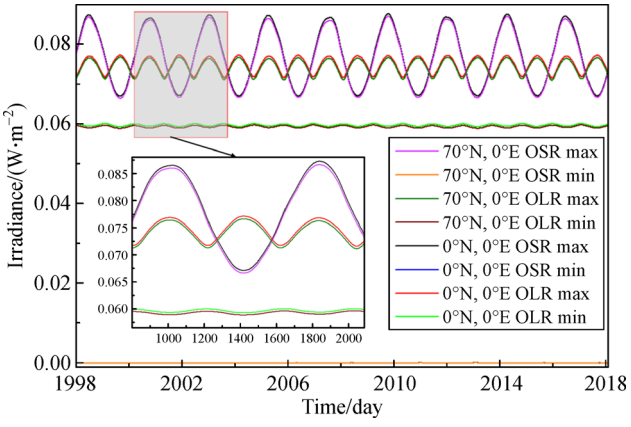

Fig. 14 The variation of the irradiance of OLR and OSR at two different locations on the 0°N, 0°E and 70°N, 0°E. This max and min represent the envelope of the OSR and OLR diurnal variation extremes, respectively.

from the value at the reference point 0°E, 0°N is less than 1%. Figure 15 shows the change curve of irradiance for each degree of latitude change on 0°E longitude, and $f_1(\theta)$, $f_2(\theta)$, and $f_3(\theta)$ represent OLR monthly average value, OSR monthly average value and OSR monthly max value, respectively. It can be seen from Fig. 15 that the farther from the reference point, the greater the change in OSR and OLR, but the change of irradiance corresponding to each degree of latitude change is small, ranging from 0.001 to 0.011 $\mathrm{mW \cdot m^{-2} \cdot deg^{-1}}$ at the reference point and 80°N, 0°E.

From the previous analysis (Figs. 10–13), it can be seen that when the moon-based earth observation is performed in the region 65°W–65°E and 65°S–65°N, the relative deviation of the irradiance is less than 0.4%. In other words, the deviation caused by the lunar position is not more than 0.31 and 0.35 $\mathrm{mW \cdot m^{-2}}$. The difference caused by different locations in this area is smaller, so the uniformity of irradiance is better.

3.3 The North and South Poles

Due to the special geographic location, illumination, and topography of the lunar polar region, especially the discovery of water ice, the polar area has been selected as the region for lunar exploration, like “CE-6” and “CE-7.” The moon-based earth observation is an important application objective for China’s future lunar exploration program (Gerstenmaier, 2017; Lin et al., 2018; Fan et al., 2019; Li, Wang et al., 2019). If the moon-based earth observation equipment could be added to the polar region exploration project, it will provide valuable practical experience for the follow-up study of the moon-based earth observation in low latitudes. Therefore, the observation duration of the north and south poles for the earth and irradiance of the lunar polar region are analyzed. Figures 16(a) and 16(c) shows the monthly statistical distribution of the visible and invisible duration for the earth’s TOA at the lunar north and south poles from 2010 to 2030. The observation duration for the earth’s TOA presents periodic changes and the period is about 6.5 years. The invisible

Table 1 Relative deviation of different regions of the moon

Type	Region	Reference point	Average value
OLR	45°N–85°N 45°S–85°S	−0.8%–0.6%	−0.5%–0.3%
	15°N–45°N 15°S–45°S	−0.35%–0.2%	−0.8%–0.6%
	15°S–15°N	−0.05%–0	0.2%–0.3%,
OSR	45°N–85°N 45°S–85°S	−0.85%–0.5%	−0.55%–0.25%
	15°N–45°N 15°S–45°S	−0.38%–0.16%	−0.1%–0.1%
	15°S–15°N	−0.07%–0	0.2%–0.3%

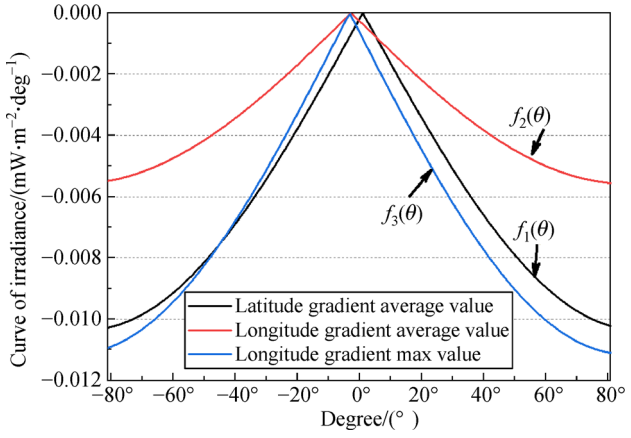

Fig. 15 The absolute deviation of the irradiance for each degree of latitude change on 0°E longitude. (Red, black and blue represent OSR monthly average Value, OLR monthly average Value, OSR monthly max Value, respectively).

duration per month is basically greater than the invisible time and only at certain times are similar, such as the end of 2013 and the end of 2019. The mean and standard deviation of the observation duration for the earth are shown in Figs. 16(b) and 16(d). The monthly mean visible and invisible time for the lunar north and south poles are equivalent, about 323 h and 408 h, respectively. However, the standard deviation varies with the month and the range of visible duration for north and south poles are 36–53 h and 38–52 h. The standard deviation and mean indicates that, from the perspective of the observable time of the earth, there is no obvious difference between the north and south regions of the moon.

The visible time ratio of north and south poles is a key factor for the design and full play of the advantages of the moon-based platform. Due to the special orbital characteristics of the earth-moon system and the moon's small axial inclination (1.54°), there is also a change in the monthly visible time ratio of the earth in the polar regions (Fig. 17). As shown in Fig. 17, the monthly visible time ratio of the polar regions ranges from 0.35–0.55 and the ratio less than 0.5 occupies the main part. Besides, the μ value of visual time ratio for normal probability plot are 0.44506 (South Pole) and 0.43906 (North Pole), respectively. In addition, if the actual effective observation elevation angle is taken into account, the observable time and ratio of the polar region may be further reduced. The statistical results of yearly observation duration for the North and South Poles from 2010 to 2030 show that the observation duration of the poles for the earth's TOA is always less than the invisible time each year. By comparing the maximum and minimum of visible time, we can find that choosing a suitable time period can increase the effective observation duration by about one month. In the following period from 2020 to 2030, the longest annual observable time for the earth's TOA at the North Pole will be in 2023 and 2028, and the longest annual observable time at the South Pole will be in 2020 and 2026.

Based on the time window shown in Figs. 16 – 18 shows the irradiance of OLR and OSR at the North and South Poles from January 2017 to December 2018. Due to the particularity of the orbits of the earth and the moon, the irradiance in the North and South Polar regions has a sudden change zone and exhibits complementary characteristics of time, and there is a time period that the earth's TOA cannot be visible by the North and South Poles at the same time. For the OSR, it shows a change with the period of years, but for OLR, the periodicity is not obvious. For the North Pole (Fig. 18(a)), the monthly extreme value of OSR increases from June each year and reaches the maximum value in January of the following year, then the irradiance decreases and reaches the minimum value in June of the following year. For the South Pole (Fig. 18(c)), the monthly extreme value of irradiance increases from January each year to a stable maximum value in April, then decreases from October and reaches a minimum value at the end of the year. As far as OLR is concerned, the change in irradiance at the two poles is not large and remains at a similar level. Over a long period of 18.6 years, the SW irradiance received at the North Pole ranges from 0 to 0.0867 $W \cdot m^{-2}$, and the LW irradiance varies from 0.0588 to 0.0766 $W \cdot m^{-2}$. The range of SW irradiance at the South

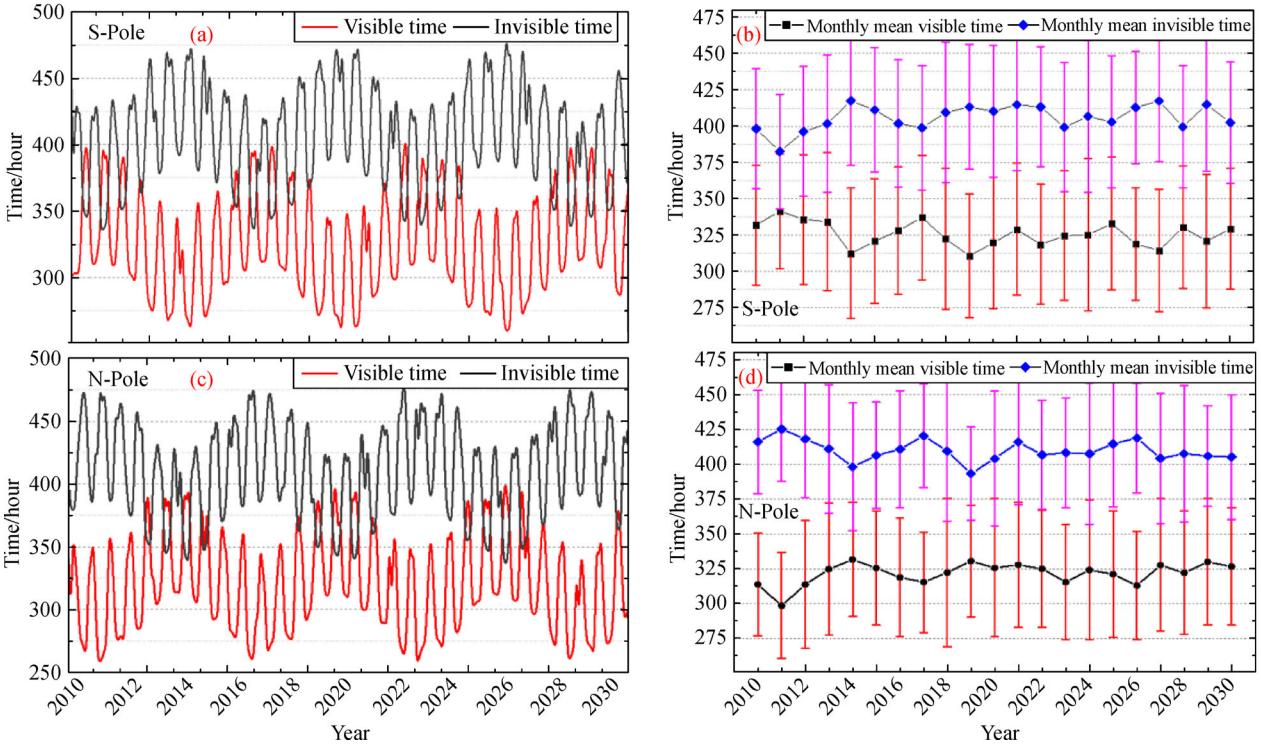

Fig. 16 (a) and (c) are the monthly observation duration of the North and South Poles from 2010 to 2030. (b) and (d) are the mean and standard deviation of the visible or invisible time for the earth.

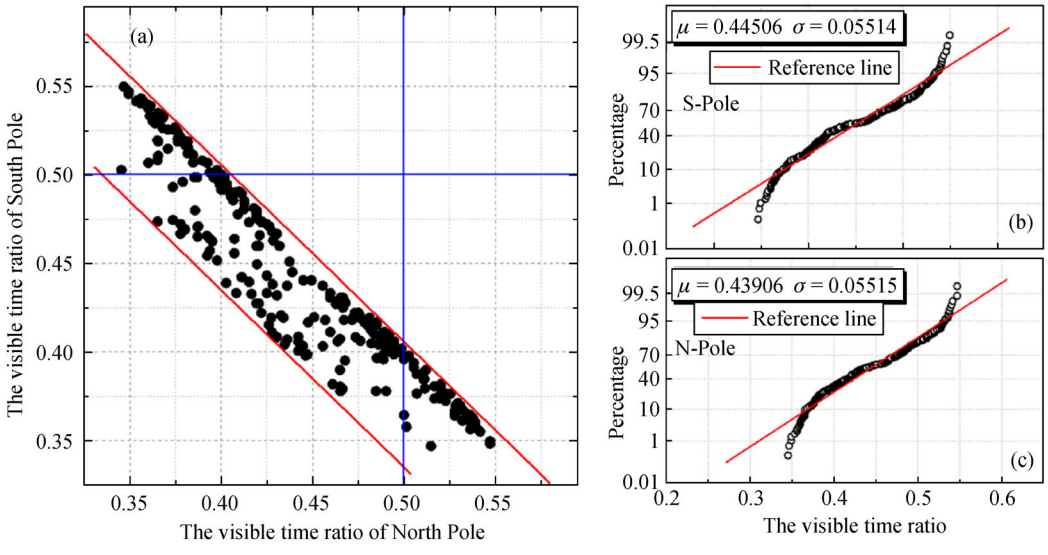

Fig. 17 (a) The monthly visible time ratio distribution of North and South Poles; (b) and (c) the normal probability plot of visual time ratio.

Pole is 0–0.0866 $W \cdot m^{-2}$, and the range of LW irradiance is 0.0588–0.0765 $W \cdot m^{-2}$. The relative deviation for OLR between the two poles and reference point ranges from 0.85% to 0.97%, and for OSR is from 0 to 1%.

3.4 Further analysis and discussion

Selecting the site (0°E, 0°N) as the reference point, the range of variation for OLR and OSR are 0.059–0.077 $W \cdot m^{-2}$ and 0–0.088 $W \cdot m^{-2}$, respectively. The irradiance is the radiation which will finally arrive at the thermal detection element of the detector. The earth radiation budget can be monitored by non-scanning wide field-of-view radiometers, or by scanning narrow field-of-view radiometers. Moreover, various types of wide-field-of-view radiometers have been launched continuously, such

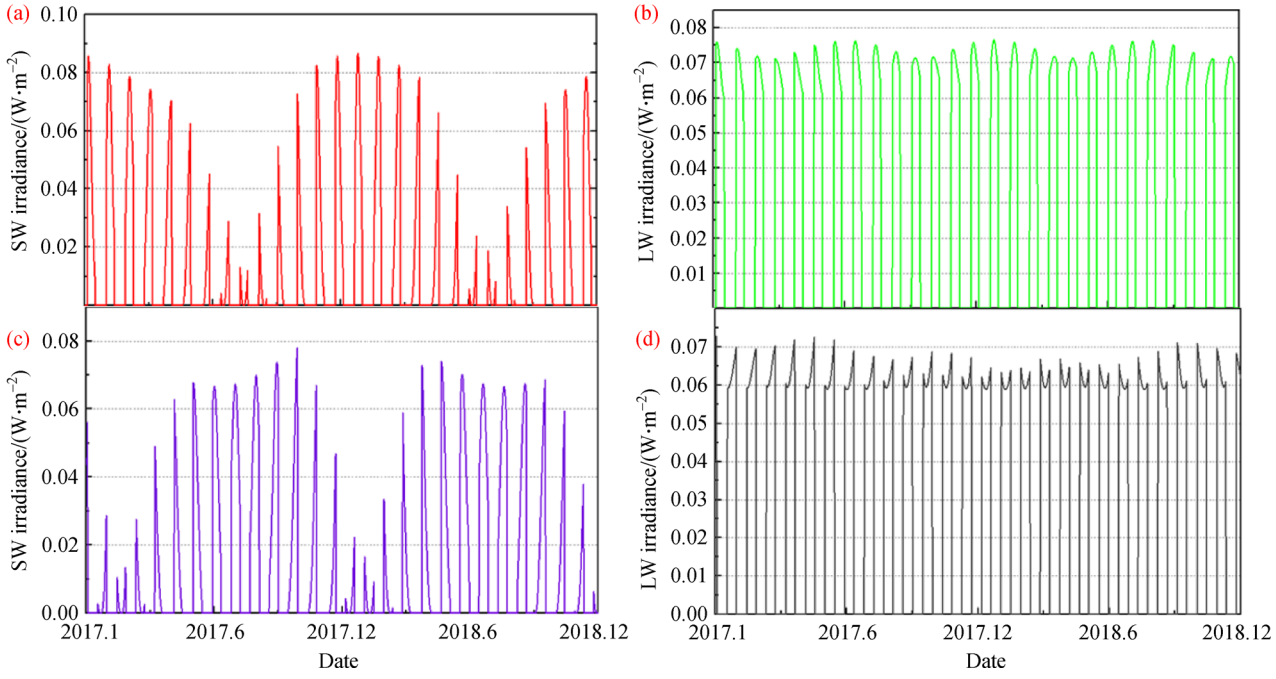

Fig. 18 The irradiance of OLR and OSR received at the North and South Pole from January 2017 to December 2018 (a) And (b) North Pole; (c) and (d) South Pole.

as Non-Scanning Broadband Earth Radiation Budget space instruments on NOAA 9 and 10 (Barkstrom and Smith, 1986), Earth Radiation Monitor on FengYun (FY)-3 series (Qiu et al., 2012), short-wave outgoing radiation monitor (IKOR) on Meteor series (Sklyarov et al., 2000), and Radiometer Assessment using Vertically Aligned Nanotubes (RAVAN) onboard a 3U CubeSat (Swartz et al., 2014). The large distance between the moon and earth lead to that outgoing radiation from earth's top of atmosphere can be measured by considering earth surface as a single pixel. Besides, the single-pixel observations can measure the radiation of the earth from limb to limb, like first dedicated broadband instruments on Nimbus 6, Nimbus 7 and ERBE, and the single-pixel wide field of view observations can mitigate the lack of temporal samples caused by orbit limitations and the error due to time interpolation (Dewitte and Clerbaux, 2017; Ye et al., 2019; Schifano et al., 2020). In addition, the wide work band also makes CCD and CMOS unusable. Therefore, the non-scanning moon-based wide field-of-view observations may be a good choice considering earth as one pixel (Schifano et al., 2020). Take the ERBE nonscanner Instrument onboard the Earth Radiation Budget Satellite as an example, the detector on ERBE is active cavity receiver type radiometer, consisting of two silver conical (an active and a reference) cavities with resistance heater windings on the outside and a specular black coating on the inside to enhance absorptivity. When irradiance punched into the silver conical inside through the field of view limiting aperture and filter system sequentially, the radiation is converted into the temperature change of the cavity, and then the temperature change is converted into an electrical signal. If the relationship between the electrical signal and the incident irradiance is known, the irradiance can be inversely calculated from the detected electrical signal. Since the earth's outgoing radiation includes wide-band long-wave radiation and wide-band short-wave radiation, so thermal detectors are selected to realize radiation detection. The choice of wavelength can be achieved by using a precisely designed filter, so as to realize the separate measurement of OLR and OSR. Its working principle is the equivalent method of electric power and thermal radiation. So, a vital issue is the achievement and maintenance of SI traceability and accurate radiometric calibration of the equipment. For moon-based earth radiation observation instrument, the SI traceability can be achieved through observing the cold and stable deep space background, using specially designed stable calibration source (such as blackbody radiation source) and the mutual correction method of the established detector network. In addition, since the early 1970s, great efforts have been made to deal with these data obtained on different height satellite platform such as the Earth Radiation Budget Satellite (ERBS) and the Clouds and the Earth's Radiant Energy System (CERES), and also developed the corresponding complete methods for estimating earth's radiation budget using satellite-based data. Therefore, the corresponding moon-based data processing method can be developed on the basis of the processing method of the satellite-based data after combining with the characteristics of the moon-based platform (Su et al., 2015, 2020).

The results show that the relative deviation of the irradiance received by different regions is less than 1%, and the OLR and OSR increased by an average of 2.11% and 1.24%, respectively, when the change of the emitted radiative fluxes on the earth's TOA is 5.00 $W \cdot m^{-2}$. The maximum values of The OLR and OSR are 0.077 and 0.088 $W \cdot m^{-2}$, respectively, so the deviation caused by the lunar position is not more than 0.77 and 0.88 $mW \cdot m^{-2}$, respectively. Assuming that the irradiance is 0.06 $W \cdot m^{-2}$, the irradiance changes of 1.25 $mW \cdot m^{-2}$ when the emitted radiative fluxes change of 5.00 $W \cdot m^{-2}$ (Fig. 7). With reference to current heat detector design technology (Rogalski, 2010; Schifano et al., 2020), and the parameter design of NISTAR, CERES, the Geostationary Earth Radiation Budget and Radiometer Assessment using Vertically Aligned Nanotubes (RAVAN) onboard a 3U CubeSat (Wielicki et al., 1996; Lorentz et al., 2019; Swartz et al., 2019), the sensitivity design goal of the MERO instrument should be better than 1 $mW \cdot m^{-2}$ in the future actual design. To achieve this sensitivity design goal, accurate measurement of the irradiance, the corresponding thermal detection element, and temperature control system must also meet certain requirements, such as high-precision temperature control and accurate photoelectric equivalent measurement (Schifano et al., 2020; Su et al., 2020). From the previous analysis (Figs. 11–14), it can be seen that when the observation is performed in the region 65°W–65°E and 65°S–65°N, the relative deviation of the irradiance is less than 0.4%. In other words, the deviation caused by the lunar position is not more than 0.31 and 0.35 $mW \cdot m^{-2}$. So selecting 2 to 3 locations in the region 65°W–65°E and 65° S–65°N to observe the earth at the same time via a network, which could perform mutual radiometric calibration. Besides, it can make full use of the angle characteristics between different platforms to improve data availability.

In this paper, we analyzed the influence of lunar surface position on irradiance of MERO by using the established radiation heat transfer model, but a limitation still exists in the model. The moon is assumed to be a sphere with a radius of 1738 km, ignoring the influence of the lunar terrain. The terrain mainly affects the position and attitude of the MERO instrument, and the visibility of the earth for MERO. Since the adjustment mechanism can ensure that the looking vector of the detector always points to the earth, the influence of the terrain on the irradiance is mainly reflected in the visibility. Since the terrain of the moon's near-side is mainly the mare and relatively flat, it has less impact on visibility. Due to the particularity of the polar position, the polar area has been selected as the region for lunar exploration (Gerstenmaier, 2017; Lin et al., 2018; Fan et al., 2019; Li et al., 2019; Flahaut et al., 2020). The visibility of the earth in the Polar Regions is relatively poor in comparison with the low-latitude regions and if the actual effective observation elevation angle is taken into account, the observable time and ratio of the polar region may be further reduced. However, if the moon-based earth observation equipment is equipped in the polar region exploration project, it not only could verify the feasibility of moon-based earth observation through real measured data, but also provide valuable practical experience for the follow-up study of earth observation in low latitudes. Moreover, in order to make full use of the advantages of the moon-based platform for earth observation, low-latitude areas should be given priority as a place for observation equipment in the follow-up projects. In addition, the purpose of this work is to analyze the impact of lunar surface position on irradiance and the focus is the size, range and regional differences of irradiance, so visibility is not included. In the next work, we will further analyze the influence of topography in moon-based earth observation from the perspective of visibility.

4 Conclusions

In this work, the influence of lunar surface position on irradiance of moon-based earth radiation observation was analyzed based on a radiation heat transfer model. To compare the spatial characteristics of the irradiance caused by positions, the site (0°E, 0°N) was selected as the reference. By comparing with NISRTAR detection data, the model was verified and the calculation results have a good consistency with the NISRTAR actual detected data. The results show that the sum of outgoing long-wave radiation (OLR) and outgoing short-wave radiation (OSR) vary from 0.059 to 0.164 $W \cdot m^{-2}$ and the period of change is about 1 year. The OLR and OSR increased by an average of 2.11% and 1.24%, respectively, when the change of the emitted radiative fluxes on earth's TOA is 5.00 $W \cdot m^{-2}$. By analyzing the spatial characteristics of the irradiance, the results show that the irradiance at different positions on the lunar surface is circular distribution. Besides, the MERO instrument that is placed in the region of 65°W–65°E and 65°S–65°N can guarantee the permanent detectability of Earth and ensure the MERO instrument detect the irradiance more effectively. The relative deviation between the reference point and the marginal area is less than 1%. In other word, the deviation of the irradiance at different lunar positions from the value at the reference point is less than 0.9 $mW \cdot m^{-2}$. With reference to NISTAR's design parameters and current heat detector design technology, the sensitivity design goal of the MERO instrument should be better than 1 $mW \cdot m^{-2}$ in the future actual design. For the lunar polar region, which is the priority for future exploration, due to the influence of the lunar libration and the precession of the lunar orbit plane, the instrument's entrance pupil irradiance changes periodically and exhibits complementary characteristics of time. The variation range of irradiance for short-wave radiation (SW) is greater than the variation ranges of long-wave (LW) radiation and the

irradiance of SW reach the maximum at different times. In addition, the length of visible time of the poles for earth's TOA is always less than the invisible time each year and the annual average of the visible duration for earth is 161.5 days every year at the polar region. The MERO at the polar region will provide valuable practical experience for the follow-up study of the moon-based earth observation in low latitudes.

Acknowledgements This work was supported by the National Natural Science Foundation of China (Grant No. 41590855). These data were obtained from the NASA Langley Research Center Atmospheric Science Data Center (available at EarthData website). We also thank NASA Jet Propulsion Laboratory for providing the free ephemeris data.

References

Barkstrom B R, Smith G L (1986). The earth radiation budget experiment: science and implementation. Rev Geophys, 24(2): 379–390

Clark L G, Anderson E C (1965). Geometric Shape Factors for Planetary-thermal and Planetary-reflected Radiation Incident Upon Spinning and Nonspinning Spacecraft (Vol. 2835). National Aeronautics and Space Administration

Dewitte S, Clerbaux N (2017). Measurement of the earth radiation budget at the top of the atmosphere—a review. Remote Sens, 9(11): 1143

Duan W, Huang S, Nie C (2019). Entrance pupil irradiance estimating model for a moon-based earth radiation observatory instrument. Remote Sens, 11(5): 583

Durante M, Cucinotta F A (2011). Physical basis of radiation protection in space travel. Rev Mod Phys, 83(4): 1245–1281

Fan W W, Yang F, Han L, Wang H M (2019). Overview of Russia's future plan of lunar exploration. Sci Tech Rev, 37(16): 6–11 (in Chinese)

Flahaut J, Carpenter J, Williams J P, Anand M, Crawford I A, van Westrenen W, Füri E, Xiao L, Zhao S (2020). Regions of interest (ROI) for future exploration missions to the lunar South Pole. Planet Space Sci, 180: 104750

Folkner W M, Williams J G, Boggs D H (2008). The planetary and lunar ephemeris DE 421. JPL IOM 343R–08–003

Gerstenmaier W (2017). Progress in defining the Deep Space Gateway and Transport Plan. In: NASA Advisory Council Human Exploration and Operations Committee Meeting

Gilmore D G (2002). Spacecraft Thermal Control Handbook (2nd eds). E1 Segundo, California: The Aerospace Corporation Press

GSFC (2008). A standardized lunar coordinate system for the lunar reconnaissance orbiter. In: LRO Project and LGCWG White Paper Version 5

Guo H, Ye H, Liu G, Dou C, Huang J (2020). Error analysis of exterior orientation elements on geolocation for a moon-based earth observation optical sensor. Int J Digit Earth, 13(3): 374–392

Guo H, Liu G, Ding Y (2018). Moon-based Earth observation: scientific concept and potential applications. Int J Digit Earth, 11(6): 546–557

Holman J P (2002). Heat Transfer (9th eds). New York: McGraw-Hill Book Company

Huang S (2008). Surface temperatures at the nearside of the moon as a record of the radiation budget of earth's climate system. Adv Space Res, 41(11): 1853–1860

Huang J, Guo H, Liu G, Shen G, Ye H, Deng Y, Dong R (2020). Spatio-temporal characteristics for moon-based earth observations. Remote Sens, 12(17): 2848

Johnson J R, Lucey P G, Stone T C, Staid M I (2007). Visible/near-infrared remote sensing of earth from the moon. In: NASA advisory council workshop on science associated with the lunar exploration architecture white papers.

Karalidi T, Stam D M, Snik F, Bagnulo S, Sparks W B, Keller C U (2012). Observing the earth as an exoplanet with LOUPE, the lunar observatory for unresolved polarimetry of earth. Planet Space Sci, 74 (1): 202–207

Kopp G (2016). Earth's incoming energy: the total solar irradiance. Comprehen Remot Sens, 5: 32–66

Li C, Wang C, Wei Y, Lin Y (2019). China's present and future lunar exploration program. Science, 365(6450): 238–239

Li T, Guo H, Zhang L, Nie C, Liao J, Liu G (2019). Simulation of moon-based earth observation optical image processing methods for global change study. Front Earth Sci, 14(2): 236–250

Liang S (2018). Volume 5 overview: recent progress in remote sensing of earth's energy budget. Comprehensive Remote Sensing, 5: 1–31

Lieske J H (1979). Precession matrix based on IAU /1976/ system of astronomical constants. Astron Astrophys, 73(3): 282–284

Lin X U, Yongliao Z O U, Yingzhuo J I A (2018). China's planning for deep space exploration and lunar exploration before 2030. Chin J Space Sci, 38(5): 591–592

Lohmeyer W Q, Cahoy K (2013). Space weather radiation effects on geostationary satellite solid-state power amplifiers. Space Weather, 11(8): 476–488

Luther M R, Cooper J E, Taylor G R (1986). The earth radiation budget experiment nonscanner instrument. Rev Geophys, 24(2): 391–399

Mudawar I (2001). Assessment of high-heat-flux thermal management schemes. IEEE Trans Compon Packag Tech, 24(2): 122–141

Pallé E, Goode P R (2009). The lunar terrestrial observatory: observing the earth using photometers on the moon's surface. Adv Space Res, 43(7): 1083–1089

Petit G, Luzum B (2016). IERS-IERS conventions (2010). In: International Earth Rotation and Reference Systems Service (IERS) Technical Note

Peyrou-Lauga R (2017). Using real earth albedo and earth IR flux for spacecraft thermal analysis. In: 47th International Conference on Environmental Systems

Qiu H, Hu L, Zhang Y, Lu D, Qi J (2012). Absolute radiometric calibration of Earth radiation measurement on FY-3B and its comparison with CERES/Aqua data. IEEE Trans Geosci Remote Sens, 50(12): 4965–4974

Rogalski A (2010). Infrared Detectors. CRC Press

Schifano L, Smeesters L, Geernaert T, Berghmans F, Dewitte S (2020). Design and analysis of a next-generation wide field-of-view earth radiation budget radiometer. Remote Sens, 12(3): 425

Sklyarov Y, Brichkov Y, Vorobyov V, Kotuma A, Fomina N (2000). Radiometric measurements from Russian Satellites Meteor-3 7 and Resurs-1. Mapp Sci Remote Sens, 37: 73–75

Stephens G L, O'Brien D, Webster P J, Pilewski P, Kato S, Li J L (2015). The albedo of Earth. Rev Geophys, 53(1): 141–163

Su W, Corbett J, Eitzen Z, Liang L (2015). Next-generation angular distribution models for top-of-atmosphere radiative flux calculation from CERES instruments: methodology. Meas Tech, 8(2): 611–632

Su W, Minnis P, Liang L, Duda D P, Khlopenkov K, Thieman M M, Yu Y, Smith A, Lorentz S, Feldman D, Valero F P J (2020). Determining the daytime earth radiative flux from National Institute of Standards and Technology Advanced Radiometer (NISTAR) measurements. Atmos Meas Tech, 13(2): 429–443

Swartz B H, Dyrud L P, Lorentz S R, Wu D L, Wiscombe W J, Papadakis S, Huang P M, Smith A, Deglau D (2014). The RAVAN CubeSat mission: progress toward a new measurement of earth outgoing radiation. In: AGU Fall Meeting Abstracts, 2014: A22F–04

Swartz W H, Lorentz S R, Papadakis S J, Huang P M, Smith A W, Deglau D M, Yu Y, Reilly S M, Reilly N M, Anderson D E (2019). RAVAN: CubeSat demonstration for multi-point earth radiation budget measurements. Remote Sens (Basel), 11(7): 796

Tsai J R (2004). Overview of satellite thermal analytical model. J Spacecr Rockets, 41(1): 120–125

Wang H, Guo Q, Li A, Liu G, Huang J (2019). Comparative study on the observation duration of the two-polar regions of the earth from four specific sites on the moon. Int J Remote Sens, 41(1), 339–352

Wielicki B A, Barkstrom B R, Harrison E F, Lee R B III, Smith G L, Cooper J E (1996). Clouds and the Earth's Radiant Energy System (CERES): an earth observing system experiment. Bull Am Meteorol Soc, 77(5): 853–868

Yang S, Tao W (2006). Numerical Heat Transfer (4th eds). Beijing: Higher Education Press: 350–439 (in Chinese)

Ye H, Guo H, Liu G, Ren Y (2018a). Observation duration analysis for earth surface features from a Moon-based platform. Adv Space Res, 62(2): 274–287

Ye H, Guo H, Liu G, Ren Y (2018b). Observation scope and spatial coverage analysis for earth observation from a moon-based platform. Int J Remote Sens, 39(18): 5809–5833

Ye H, Guo H, Liu G, Guo Q, Zhang L, Huang J (2019). Temporal sampling error analysis of the earth's outgoing radiation from a moon-based platform. Int J Remote Sens, 40(18): 6975–6992

Yuan L, Liao J (2020). A physical-based algorithm for retrieving land surface temperature from moon-based earth observation. IEEE J Sel Top Appl Earth Obs Remote Sens, 13: 1856–1866

Yuan L, Liao J (2019). Exploring the influence of various factors on microwave radiation image simulation for moon-based earth observation. Front Earth Sci, 14(2): 430–445